

Christoffer D. Hystad

**The title of your master's thesis should be
written here**

Any undertitle is written here

Master's thesis in Cybernetics and Robotics
Supervisor: Jan-Tommy Gravdahl
December 2025

Norwegian University of Science and Technology
Faculty of Information Technology and Electrical Engineering
Department of Engineering Cybernetics



ABSTRACT

Write an abstract/summary of your thesis, and state your main findings here.

A summary should be included in both English and any second language, if this is applicable, regardless if the thesis is written in English or in your preferred language. These should be on separate pages, the English version first.

PREFACE

Write the preface of your thesis here.

You may include acknowledgements and thanks as part of your preface on this page, or you may add it as a new chapter after the preface.

CONTENTS

Abstract	i
Preface	ii
Contents	iii
List of Figures	vii
List of Tables	viii
1 Introduction	1
1.1 Background & Motivation	1
1.2 Problem Definition	3
1.2.1 Project Formulation	3
1.3 Overall Method	4
1.4 Project Scope & Limitations	4
1.4.1 Simulation Configuration Scope	4
1.4.2 Perturbation Modelling Scope	4
1.4.3 Propagation Tool Scope	4
1.4.4 Limitations	5
1.5 Report Structure	5

2 Literature Review	6
2.1 Orbital Propagation	7
2.1.1 Analytical Propagation (Simplified General Perturbations 4 (SGP4))	7
2.1.2 Numerical Orbit Propagation	10
2.1.3 Semianalytical and Hybrid Propagators	10
2.1.4 Propagator Comparison and Validation	10
2.2 Orbital Perturbation Modelling	10
2.2.1 Gravity-Field Perturbations	10
2.2.2 Atmospheric Drag	10
2.2.3 Solar Radiation Pressure	10
2.2.4 Third-Body Perturbations	10
2.3 Error Growth and Propagation Stability	10
2.3.1 Long-Term Orbit Prediction Accuracy	10
2.3.2 Sensitivity to Force-Model Fidelity	10
2.3.3 Numerical Integration Error	10
2.3.4 Regime-Dependent Error Growth	10
2.4 Satellite Formation Flying and Relative Motion	10
2.4.1 Relative Motion Dynamics	10
2.4.2 Sensitivity of Relative Motion to Propagation Error	10
2.4.3 Formation-Keeping delta-V Requirements	10
2.4.4 Disturbance Effects on Formation Stability	10
2.5 Summary of Literature Review	10
3 Theory	14
3.1 Reference Frames	14
3.1.1 Earth-Centered Inertial (ECI) Frame	15
3.1.2 Radial-Transverse-Normal (RTN) Frame	15

3.1.3	Earth-Fixed Earth-Centered (ECEF) Frame	15
3.2	Orbital Perturbations	16
3.2.1	Spherical Harmonics	16
3.2.2	Atmospheric Drag	18
3.2.3	Solar Radiation Pressure	19
3.2.4	Third-Body Perturbations	20
3.3	Numerical Orbit Propagation	21
3.4	Analytical Orbit Propagation - SGP4	21
4	Methods	22
4.1	Simulation Design	22
4.2	Literature Search Methodology	22
4.3	Software Development	22
4.3.1	Software Architecture	22
5	Results	25
5.1	Simulation Parameters	25
5.2	Prelim results	25
5.2.1	Simulator output difference plots	26
5.2.2	R	26
6	Discussion	27
6.1	Future work	27
7	Conclusions	28
	References	29
	Appendices:	32
	A - Github repository	33

B - Numerical Values	34
-----------------------------	-----------

LIST OF FIGURES

1.1.1 Launch cost per kilogram to LEO versus first launch date, courtesy of [2]	1
3.1.1 Illustration of the Earth-Centered Inertial (\mathcal{F}^i) and Radial-Transverse-Normal (\mathcal{F}^r) frames used in this project. The unit vectors have different length for illustrative purposes. Adapted from [18, 19]	14
3.2.1 Order of magnitude of various perturbations of a satellite orbit. Courtesy of [21]	16
3.2.2 Tidal forces due to the gravitational attraction of a distant point-like mass. Courtesy of [21]	20

LIST OF TABLES

2.5.1 Literature overview for the <i>Orbital propagation</i> theme	11
2.5.2 Literature overview for the <i>Orbital perturbation modelling</i> theme	12
2.5.3 Literature overview for the <i>Error growth & propagation stability</i> theme . .	12
2.5.4 Literature overview for the <i>Satellite formation flying</i> theme	13
3.2.1 Zonal coefficients and associated Legendre polynomials up to fourth degree. Values courtesy of [23].	18
5.1.1 Physical constants and associated numerical value. J -terms courtesy of [23].	25
.0.1 Physical constants and associated numerical value. J -terms courtesy of [23].	34

CHAPTER ONE

INTRODUCTION

1.1 Background & Motivation

Global Navigation Satellite Systems (GNSS) have become deeply embedded into our modern infrastructure with multiple constellations, such as GPS, GLONASS, Galileo and BeiDou, ensuring that four satellites are observable from the surface at any given time, thus providing worldwide coverage [1]. The sheer number of operational satellites that broadcast GNSS signals makes it one of the most powerful signals of opportunity for remote sensing, enabling monitoring without the need for onboard transmitters.

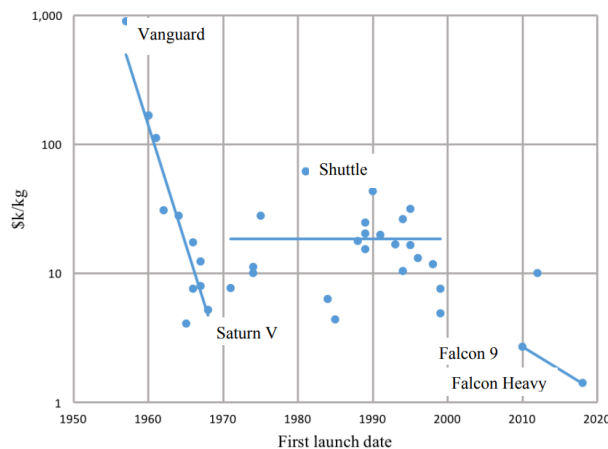


Figure 1.1.1: Launch cost per kilogram to LEO versus first launch date, courtesy of [2]

At the same time, the space sector has recently undergone rapid changes. Launch costs have fallen significantly due to government outsourcing of launch providers to private companies, and the competitive environment it produced. This is clearly shown in figure 1.1.1, where the per-kilogram launch cost has hit an all-time low with the deployment of

SpaceX rockets *Falcon 9* and *Falcon Heavy* [2]. As a result, it has become increasingly feasible for universities, research groups and smaller nations to deploy space-based systems dedicated to leveraging GNSS signals for remote sensing applications.

In parallel with this growth, there has also been an increase in the frequency of reported intentional GNSS interference to disrupt aviation operations. The interference can be divided into separate categories characterized by their difference in method and effect: *Jamming* refers to the relative high-power emission of Radio Frequency (RF) noise to block GNSS signals, while *spoofing* is the transmission of signals that resemble those from real satellites, misleading the GNSS receiver to think it has a different position [3]. The Norwegian Defense Research Establishment (FFI) states that: "In Norway's northernmost county of Finnmark, close to the Russian border, loss of GNSS signals due to jamming occurs nearly daily. [...] The number of disruptions has increased significantly since Russia's invasion of Ukraine in 2022." [4]. Data from *gpsjam.org* suggest that similar disruptions have been reported across Eastern Europe, the Middle East, and the Arctic [5]. These events highlight a broader geopolitical trend: GNSS interference is becoming more common. This places increased strategic value on systems that can detect and localize jamming and spoofing events.

GNSS Reflectometry (GNSS-R) offers a promising technique for addressing these challenges. According to Jin and Komjathy [6], Hall and Cordey [7] were the first to propose that GNSS L-band reflections could be exploited in a bistatic radar configuration to retrieve ocean surface properties, laying the foundation for modern GNSS-R techniques. Recent theory suggests that the same bistatic configuration can be used for surveillance of the GNSS spectrum, where multiple GNSS-R satellites in formation can detect and localize sources of jamming and spoofing. This emerging use-case is one of the central research goals of NTNU SmallSat Lab's GNSS-R project, which aim to develop methods for this process [8]. The project currently investigates this concept through its GNSS-R satellite mission study, exploring formations geometries, orbit configurations and system designs that would enable robust detection of GNSS interference sources and ships.

Accurate knowledge of spacecraft position and velocity is essential for the performance of any GNSS-R system. In such systems, regardless of application, the reflected GNSS signal is interpreted by comparing its time delay and Doppler shift relative to the direct signal. This process is highly sensitive to the specular reflection point's geolocation, which is given by the geometric relationship between the GNSS transmitter, the reflecting surface and the receiver. Even small errors in the satellite's propagated state shifts the estimated specular point by kilometers. Such errors can lead to misinterpretations of the delay-Doppler maps, for instance if the predicted specular point is over ocean when the true specular point occurs over land [9].

In real missions, the satellite orbit and relative geometry within satellite formations will naturally drift over time due to orbital perturbations. During mission design, simulation tools are used to predict the satellites motion. If the simulation does not accurately model the relevant perturbations, its predicted state evolution will diverge from physically realistic behavior, eventually yielding incorrect specular point locations and misleading conclusions about the performance of the GNSS-R system. Furthermore, inaccuracies in position and velocity directly translates to uncertainty in later analyses, like coverage analysis, or formation-keeping delta-V estimation. For these reasons, a high-fidelity

propagator is necessary to ensure realistic and reliable evaluations of the GNSS-R system performance.

1.2 Problem Definition

A system simulator has already been developed to support the development of SmallSat Lab’s GNSS-R project (cite???). The tool currently allows area coverage estimation and a detection probability analysis of a stationary maritime target, and is intended to be extended for ocean surveillance and GNSS Radio Frequency interference (RFI) detection in the future. As explored in the previous section, these analyses rely on accurately propagating both GNSS and GNSS-R satellites to minimize their uncertainties. Currently, the simulator uses the SGP4 propagator through the Skyfield Python library for this purpose.

The SGP4 propagator has long been the industry standard for orbit prediction, and has subsequently been the subject of thorough evaluation. Several studies document that the propagator can exhibit decreasing accuracy over longer time-horizons, particularly for formation-flight or precision geometry applications [10]. This raises concerns about whether the current SGP4-based implementation is sufficiently accurate for GNSS-R studies, which are highly sensitive to orbital state errors.

1.2.1 Project Formulation

This motivates a systematic verification of the Skyfield-SGP4 implementation by comparing its long-term predictions against a propagator with higher modeling fidelity. Therefore, this specialization project will support the SmallSat Lab GNSS-R mission by developing such a propagator within the Basilisk simulation framework, which natively supports detailed perturbation models and allows for controlled comparisons with Skyfield-SGP4. The study uses this capability to evaluate the differences between the propagators and evaluate their implications for GNSS-R mission analysis. As a result, the project is guided by three research questions:

- What is the intrinsic numerical difference between the Skyfield-SGP4 and the Basilisk frameworks when configured identically?
- How does the introduction of extended perturbation models influence the divergence between the propagators over time?
- How do differences in simulated translational states affect formation-keeping delta-V analyses?

Answering these questions will support the project’s goal of guaranteeing the reliability and accuracy of orbital propagation tools used for GNSS-R small-satellite formation studies in future mission design.

1.3 Overall Method

1.4 Project Scope & Limitations

This specialization project focuses on evaluating the long-term orbital propagation accuracy of two distinct simulation frameworks, Skyfield-SGP4 and a high-fidelity Basilisk propagator, in the context of GNSS-R formation-flying missions. To ensure a controlled and way defined comparison, the project's scope has been limited to a set of simulation configurations and perturbation models.

1.4.1 Simulation Configuration Scope

The analysis covers a relatively long time-horizon, ranging from several days up to one week, in order to adequately capture the frameworks' divergence over a mission-relevant time span. The simulated formation consists of two satellites flying in Low Earth Orbit (LEO) in a leader-follower configuration. Both are initialized on the same orbital plane with nominally constant along-track separation and with the same initial conditions to guarantee same-case comparisons.

1.4.2 Perturbation Modelling Scope

The Basilisk propagator incorporates a selection of the most influential orbital perturbation effects in LEO:

- Earth's gravity field represented through J2-J4 spherical harmonics,
- Atmospheric drag using an exponential density model,
- Cannonball Solar Radiation Pressure (SRP) model with a fixed reflectivity coefficient, and
- third-body gravitational pull from the Sun and Moon

1.4.3 Propagation Tool Scope

The Skyfield-SGP4 implementation serves as the baseline, while Basilisk is used as the higher-fidelity reference. Each framework is configured to propagate identical initial conditions, allowing direct numerical comparison of state evolution over the defined time interval.

1.4.4 Limitations

Several aspects of GNSS-R mission analysis lie outside the scope of this specialization project. First, no attitude dynamics are modeled. The satellites are assumed to maintain a fixed nadir-oriented attitude or otherwise idealized pointing, which removes attitude-orbit coupling and optical or RF pointing constraints from consideration.

Second, the project includes no GNSS-R signal modeling or bistatic radar simulation. The study evaluates orbital geometry only; signal processing elements such as delay-Doppler map generation, specular-point reflectivity, link budget modeling, or interference detection algorithms fall beyond the project's objectives.

Third, no active formation-keeping control is implemented. The satellites follow purely ballistic trajectories under the applied perturbations. As such, the delta-V analysis is limited to estimating how often and how strongly formation drift would need to be corrected, rather than simulating actual guidance, navigation, and control (GNC) actions.

Finally, conclusions drawn from this study are limited to the tested scenarios. The orbital regimes, perturbation models, and formation geometry considered here may not generalize to all LEO missions, nor to GNSS-R concepts employing different formation layouts, attitude profiles, or operational constraints.

These limitations naturally define the boundary between the present specialization project and a potential master's thesis. While this project focuses on verifying orbital propagation fidelity, a master's thesis could extend the analysis by incorporating full attitude modeling, GNSS-R signal simulation, operational formation-keeping strategies, and end-to-end detection performance. Such expansions would build upon the validated propagation models developed here, enabling a more comprehensive assessment of GNSS-R formation-flying missions.

1.5 Report Structure

Following is a brief overview of chapters in this report, and what each of them cover.

CHAPTER
TWO

LITERATURE REVIEW

Although astrodynamics is rooted in centuries of celestial mechanics, it only recently emerged as a distinct scientific discipline. As outlined by Szebehely's historical account of the field [11], the development of astrodynamics may be divided into four broad periods: the pre-Newtonian era, the classical or Newtonian period, the contributors from the nineteenth century and finally the rapid expansion that took place in the twentieth century. Although its conceptual roots stretch back to ancient astronomers such as Aristotle and Hipparchus, and its mathematical foundations were laid by Newton's *Principia* [12], Szebehely emphasizes that the practical astrodynamics discipline concerned with applying celestial and ballistic mechanics to artificial bodies, was only formed in the early 1930s. Following the second world war, the field saw rapid growth due to Soviet launch of the *Sputnik* satellite in 1957, and the ensuing space race. With the introduction of more powerful digital computers in the 1960s, Brouwer, Herrick and others led research teams that laid the foundation for analytical and numerical orbit propagation.

Building on this historical foundation, the field has continued to evolve through substantial research effort aimed at increasing predictive accuracy. This trend is indicated by the sharp increase in published work since the early 1990s proposing improved numerical integration methods, orbital propagation schemes and disturbance models. This chapter therefore provides an overview of the theoretical foundations and prior research relevant to this project that have been published after 1960. To provide structure while keeping the scope focused, the review is divided into four themes, each covering aspects of astrodynamics whose understanding is essential for addressing the research questions presented in Section ???. The first theme covers analytical and numerical orbital propagation methods and studies assessing their intrinsic accuracy. The second theme examines orbital perturbation models, specifically gravity-field perturbations, atmospheric drag and SRP. These two themes together provide the methodological background for understanding the differences between the Skyfield SGP4 baseline and the relatively high-fidelity Basilisk implementations.

The third theme envelops the error growth and propagation stability of propagators with a

focus on long-term orbit prediction accuracy, sensitivity to perturbation-model fidelity and numerical integration error. Finally, the forth theme covers satellite formation-keeping, and reviewing how absolute propagation error translate into inaccuracies in relative-state predictions and, consequently, into differences in delta-V estimates for formation maintenance. The last two themes is directly related to the project's investigation of how simulator differences evolve over time, and will provide the theory necessary to understand discrepancies between propagations.

The purpose of this literature review is to map the existing knowledge that supports the analysis carried out in this project. The aim is not to identify research gaps or propose new theoretical developments, but rather provide the theoretical background needed to understand the propagation methods, orbital perturbations and mechanisms causing prediction error over longer time-horizons, which are covered in depth in chapter 3. This mapping of established models and methods also serves to contextualize their relative accuracies, forming the foundation for the simulation-based comparison presented in later chapters.

2.1 Orbital Propagation

2.1.1 Analytical Propagation (SGP4)

Analytical orbit propagation methods rely on closed-form or series-based approximations of the perturbing forces acting on an artificial satellite. Among these, the SGP4 algorithm is the most widely used and has become the de facto standard for propagating publicly distributed Two-Line Element (TLE) sets. As described in detail by Vallado [13], SGP4 operates on mean orbital elements rather than osculating elements, and applies a sequence of analytical corrections to account for dominant perturbations. These corrections include secular and periodic contributions from the Earth's oblateness, simplified treatments of atmospheric drag, and, in some cases, resonance effects. Because the dynamics are expressed through closed-form perturbation series, SGP4 achieves exceptional computational speed and remains efficient even when used to propagate thousands of objects, which has contributed significantly to its long-standing operational use.

Despite these advantages, the analytical nature of SGP4 introduces several well-known limitations. Since the algorithm uses simplified perturbation models and a low-fidelity representation of atmospheric drag, its accuracy deteriorates over longer time horizons, especially in low Earth orbit where drag and solar radiation pressure can drive significant deviations from the mean-element trajectory. Liu *et al.* [14] demonstrate this behaviour empirically, showing that the difference between SGP4 predictions and high-fidelity numerical ephemerides grows noticeably with propagation time. Their work further illustrates how machine-learning techniques can be used to correct these long-term deviations, highlighting the underlying structural limitations of the analytical model. Similarly, Conkey and Zielinski [15] compare classical SGP4 with the extended-precision SGP4-XP variant, showing that improved analytical treatments of atmospheric drag, resonance terms and solar radiation pressure can offer measurable accuracy gains, particularly outside low Earth orbit.

More broadly, studies comparing with high-precision numerical propagators provide valuable insight into the intrinsic accuracy of analytical propagation. Acciarini *et al.* [16] analyse the divergence between SGP4 and a high-fidelity numerical integrator that models detailed perturbations, demonstrating that the differences become increasingly significant over multi-day time spans. Their findings reinforce a key conclusion from the broader literature: while SGP4 is sufficiently accurate for short-term prediction and catalog maintenance, its underlying modelling assumptions impose fundamental limits on long-term orbit fidelity.

In this project, the `Skyfield` Python library is used to provide a baseline trajectory representation, and its implementation relies directly on SGP4 for propagating TLE-based initial conditions. As a result, the SGP4 model serves as the analytical benchmark against which the extended high-fidelity `Basilisk` simulations are compared in later chapters.

2.1.2 Numerical Orbit Propagation

2.1.3 Semianalytical and Hybrid Propagators

2.1.4 Propagator Comparison and Validation

2.2 Orbital Perturbation Modelling

2.2.1 Gravity-Field Perturbations

2.2.2 Atmospheric Drag

2.2.3 Solar Radiation Pressure

2.2.4 Third-Body Perturbations

2.3 Error Growth and Propagation Stability

2.3.1 Long-Term Orbit Prediction Accuracy

2.3.2 Sensitivity to Force-Model Fidelity

2.3.3 Numerical Integration Error

2.3.4 Regime-Dependent Error Growth

2.4 Satellite Formation Flying and Relative Motion

2.4.1 Relative Motion Dynamics

2.4.2 Sensitivity of Relative Motion to Propagation Error

2.4.3 Formation-Keeping delta-V Requirements

2.4.4 Disturbance Effects on Formation Stability

2.5 Summary of Literature Review

Table 2.5.1: Literature overview for the *Orbital propagation* theme

Field	Literature
Analytical propagation (SGP4)	Vallado (2021) Liu <i>et al.</i> (2021) Conkey & Zielinski (2022) Acciarini <i>et al.</i> (2024)
Numerical orbit propagation	Brouwer & Clemence (1961) Bate, Mueller & White (1971) Battin (1999) Montenbruck & Gill (2000) Vallado (2025)
Semianalytical / hybrid propagators	Kaula (1966) Conkey & Zielinski (2022) Wang <i>et al.</i> (2024)
Propagator comparison & validation	Roscoe <i>et al.</i> (2014) Liu <i>et al.</i> (2021) Conkey & Zielinski (2022) Acciarini <i>et al.</i> (2024) Vallado (2025)

Table 2.5.2: Literature overview for the *Orbital perturbation modelling* theme

Field	Literature
Gravity-field perturbations	Kaula (1966) Battin (1999) Montenbruck & Gill (2000) Wakker (2015) Vallado (2021) Wang <i>et al.</i> (2024)
Atmospheric drag	Montenbruck & Gill (2000) Roscoe <i>et al.</i> (2014) Vallado (2021)
Solar radiation pressure (SRP)	Wertz (1978) Montenbruck & Gill (2000) Roscoe <i>et al.</i> (2014) Vallado (2021)
Third-body perturbation	Wertz (1978) Montenbruck & Gill (2000) Roscoe <i>et al.</i> (2014) Vallado (2021)

Table 2.5.3: Literature overview for the *Error growth & propagation stability* theme

Field	Literature
Long-term orbit prediction accuracy	Liu <i>et al.</i> (2021) Conkey & Zielinski (2022) Acciarini <i>et al.</i> (2024) Vallado (2025)
Sensitivity to force-model fidelity	Roscoe <i>et al.</i> (2014) Vallado (2021) Conkey & Zielinski (2022) Acciarini <i>et al.</i> (2024) Wang <i>et al.</i> (2024)
Numerical integration error	Bate, Mueller & White (1971) Battin (1999) Montenbruck & Gill (2000) Vallado (2021)
Regime-dependent error growth	Roscoe <i>et al.</i> (2014) Conkey & Zielinski (2022) Vallado (2025)

Table 2.5.4: Literature overview for the *Satellite formation flying* theme

Field	Literature
Relative motion dynamics	Montenbruck & Gill (2000) Schaub & Junkins (2003) Kristiansen <i>et al.</i> (2007)
Sensitivity of relative motion to propagation error	Kristiansen <i>et al.</i> (2007) Roscoe <i>et al.</i> (2014) Vallado (2021)
Formation-keeping ΔV requirements	Kristiansen <i>et al.</i> (2007) Roscoe <i>et al.</i> (2014)
Disturbance effects on formation stability	Kristiansen <i>et al.</i> (2007) Roscoe <i>et al.</i> (2014)

CHAPTER
THREE

THEORY

3.1 Reference Frames

A reference frame is uniquely described by $\mathcal{F}^{rf} : \{\mathcal{O}_{rf}; \hat{\mathbf{x}}_{rf}, \hat{\mathbf{y}}_{rf}, \hat{\mathbf{z}}_{rf}\}$ where \mathcal{O}_{rf} is the origin, and $\{\hat{\mathbf{x}}_{rf}, \hat{\mathbf{y}}_{rf}, \hat{\mathbf{z}}_{rf}\}$ denote the dextral orthogonal unit vectors [17]. In this work, mainly two reference frames are used: the Earth-Centered Inertial (ECI) frame and the Radial-Transverse-Normal (RTN) frame, which is illustrated by figure 3.1.1. The ECI frame is the inertial frame used to express all absolute satellite motion about the Earth, while the RTN frame provides a satellite-centered frame of reference suited for expressing relative motion within a formation. Lastly, because gravitational and geophysical models are naturally defined in an Earth-fixed coordinate system, a third frame, the Earth-Centered Earth-Fixed (ECEF) frame, is also introduced.

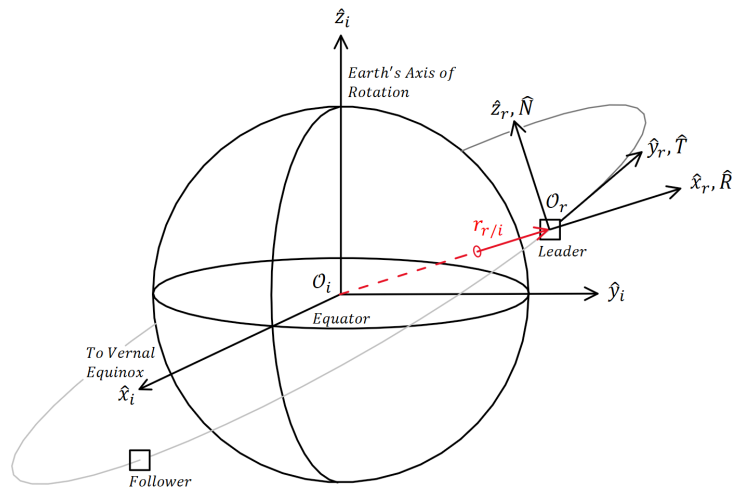


Figure 3.1.1: Illustration of the Earth-Centered Inertial (\mathcal{F}^i) and Radial-Transverse-Normal (\mathcal{F}^r) frames used in this project. The unit vectors have different length for illustrative purposes. Adapted from [18, 19]

3.1.1 Earth-Centered Inertial (ECI) Frame

The ECI frame, $\mathcal{F}^i : \{\mathcal{O}_i ; \hat{\mathbf{x}}_i, \hat{\mathbf{y}}_i, \hat{\mathbf{z}}_i\}$, has its origin at the Earth's Center of Mass (CM) and fixed principal axes relative to the celestial sphere. At any given time, $\hat{\mathbf{x}}_i$ points towards the Vernal Equinox, per definition striking through the equator. $\hat{\mathbf{z}}_i$ points along the Earth's axis of rotation through its geographical North-Pole, and $\hat{\mathbf{y}}_i$ is defined using the right-hand rule. An illustration showing this principal axis configuration is shown in figure 3.1.1. The position of an arbitrary satellite, s , relative to the Earth's CM can then be expressed by its principal components in the ECI frame with the following notation:

$$\mathbf{r}_{s/i}^i = a\hat{\mathbf{x}}_i^i + b\hat{\mathbf{y}}_i^i + c\hat{\mathbf{z}}_i^i = [a \ b \ c]^T \quad (3.1)$$

3.1.2 Radial-Transverse-Normal (RTN) Frame

The RTN frame, $\mathcal{F}^r : \{\mathcal{O}_r ; \hat{\mathbf{x}}_r, \hat{\mathbf{y}}_r, \hat{\mathbf{z}}_r\}$, is defined with its origin at the leader's CM in a leader-follower satellite formation. Using l to denote the leader satellite, the frame's orthogonal dextral unit vectors can be defined in the ECI frame as:

$$\hat{\mathbf{R}}^i = \hat{\mathbf{x}}_r^i = \frac{\mathbf{r}_{l/i}^i}{\|\mathbf{r}_{l/i}^i\|}, \quad \hat{\mathbf{N}}^i = \hat{\mathbf{z}}_r^i = \frac{\mathbf{r}_{l/i}^i \times \mathbf{v}_{l/i}^i}{\|\mathbf{r}_{l/i}^i \times \mathbf{v}_{l/i}^i\|}, \quad \hat{\mathbf{T}}^i = \hat{\mathbf{y}}_r^i = \hat{\mathbf{z}}_r^i \times \hat{\mathbf{x}}_r^i \quad (3.2)$$

Here, $\hat{\mathbf{x}}_r^i$ is the radial unit vector, pointing outwards along the leader's position vector. $\hat{\mathbf{z}}_r^i$ points in the direction orthogonal to $\{\mathbf{r}_{l/i}^i, \mathbf{v}_{l/i}^i\}$ and corresponds to the cross-track direction. Finally, $\hat{\mathbf{y}}_r^i$ is defined through the right-hand rule, giving the along-track direction. An illustration of these definitions is presented in figure 3.1.1. Using this definition, the transformations to ECI from RTN and back is given by:

$$\mathbf{R}_r^i = [\hat{\mathbf{x}}_r^i \ \hat{\mathbf{y}}_r^i \ \hat{\mathbf{z}}_r^i], \quad \mathbf{R}_i^r = (\mathbf{R}_r^i)^T \quad (3.3)$$

3.1.3 Earth-Fixed Earth-Centered (ECEF) Frame

The ECEF frame, $\mathcal{F}^f : \{\mathcal{O}_f ; \hat{\mathbf{x}}_f, \hat{\mathbf{y}}_f, \hat{\mathbf{z}}_f\}$, is a rotating Earth-fixed frame with its origin at the Earth's CM. The axis $\hat{\mathbf{z}}^f = \hat{\mathbf{z}}^i$ aligns with the Earth's mean rotation axis, $\hat{\mathbf{x}}^f$ lies on the intersection of the equator and prime meridian, and $\hat{\mathbf{y}}^f$ follows by the right-hand rule. Because the frame rotates with the Earth, the transformation between ECI and ECEF depends on time. This work adopts the formulation of Stryjewski [20], expressing the rotation about the inertial $\hat{\mathbf{z}}^i$ -axis through a time-varying angle $\theta(t)$, which is zero at the J2000 epoch (1 January 2000, 12:00 TT). The corresponding rotation matrix is

$$\mathbf{R}_i^f = \begin{bmatrix} \cos \theta(t) & -\sin \theta(t) & 0 \\ \sin \theta(t) & \cos \theta(t) & 0 \\ 0 & 0 & 1 \end{bmatrix}, \quad \mathbf{R}_f^i = (\mathbf{R}_i^f)^T \quad (3.4)$$

with the rotation angle defined as

$$\theta(t) = \omega (GMST(t) - (UT1(t) - UTC(t))), \quad \omega = 0.261799387799149 \text{ rad/h.} \quad (3.5)$$

3.2 Orbital Perturbations

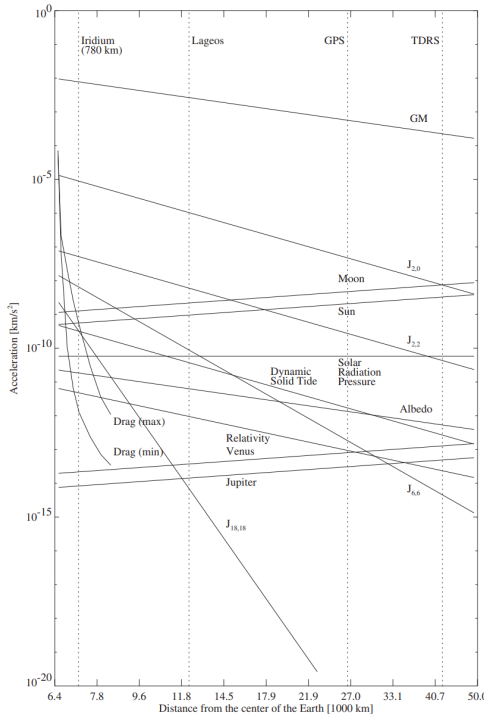


Figure 3.2.1: Order of magnitude of various perturbations of a satellite orbit. Courtesy of [21]

3.2.1 Spherical Harmonics

Assuming the Earth's mass is concentrated in the ECI frame's origin, the acceleration experienced by a spacecraft, s , can be modelled using Newton's gravitational law:

$$\mathbf{a}_{grav} = (\ddot{\mathbf{r}}_{s/i})_{grav} = -\frac{\mu}{||\mathbf{r}_{s/i}||_2^3} \mathbf{r}_{s/i} \iff (\ddot{\mathbf{r}}_{s/i})_{grav} = \nabla U, \quad \text{where } U = \mu \frac{1}{||\mathbf{r}_{s/i}||_2} \quad (3.6)$$

Here $\mu = GM$ is the Earth's gravitational parameter, and ∇U is an equivalent representation given by the gradient of the gravity potential. Other literature define U with the opposite sign, but here $U > 0$ is chosen to stay consistent with the convention used by Montenbruck & Gill. Their literature explains that this model is inaccurate due to the Earth's mass being unhomogeneously distributed through its volume, and because its rotational velocity causes its shape to bulge around the equator [21]. They go on to present an extension of equation 3.6 to account for these irregularities in the Earth's gravitational field, starting with a generalization of the gravity potential by summing up the contributions from all internal mass elements. With $\rho(\mathbf{r}_{p/i}^f)$ representing the density at some point p , and $\{\mathbf{r}_{s/i}^f, \mathbf{r}_{p/i}^f\}$ denoting the positions of the satellite and the point in ECEF respectively, the general gravity potential can be expressed as:

$$U = G \int \frac{1}{||\mathbf{r}_{s/i}^f - \mathbf{r}_{p/i}^f||_2} dm = G \int \frac{1}{||\mathbf{r}_{s/i}^f - \mathbf{r}_{p/i}^f||_2} \rho(\mathbf{r}_{p/i}^f) d^3 \mathbf{r}_{p/i}^f \quad (3.7)$$

However, the density distribution is not accurately known, which makes the expression impractical. To evaluate the integral further, the fraction can be expanded using a series of Legendre polynomials. The general Legendre polynomial P_{nm} of degree n and order m is defined as:

$$P_{nm}(u) = (1 - u^2)^{m/2} \frac{d^m}{du^m} P_n(u) \quad (3.8)$$

Introducing the spacecraft's geocentric distance $r = \|r_{s/i}\|_2$, the latitude ϕ^f and the longitude λ^f allows the satellite's position in the ECEF frame to be expressed in spherical coordinates $\{r, \phi^f, \lambda^f\}$. The superscript f is in this case used to indicate that the angles are Earth-fixed. Using these coordinates together with the associated Legendre polynomials, the gravity potential can be written in its general spherical harmonic form:

$$U = \frac{\mu}{R} \sum_{n=0}^{\infty} \sum_{m=0}^n (C_{nm} V_{nm} + S_{nm} W_{nm}), \begin{cases} V_{nm} = \left(\frac{R}{r}\right)^{n+1} P_{nm}(\sin \phi^f) \cdot \cos m \lambda^f \\ W_{nm} = \left(\frac{R}{r}\right)^{n+1} P_{nm}(\sin \phi^f) \cdot \sin m \lambda^f \end{cases} \quad (3.9)$$

Here, R denote the Earth's reference radius, and the geopotential coefficients C_{nm} and S_{nm} encode the internal mass distribution's effect on the satellite. Because the longitudinal mass variations are comparatively small, a common simplification is to set $m = 0$, giving the so-called zonal coefficient. Under this assumption, $J_n = -C_{n0}$ and $W_{n0} = 0$, which significantly simplifies the equation 3.9. Using the zonal terms up to forth degree, the truncated gravitational potential can be computed from the Legendre polynomials and J -terms in table 3.2.1:

$$\begin{aligned} U(r, \phi^f, \lambda^f) &= \frac{\mu}{R} \sum_{n=0}^4 (C_{n0} V_{n0} + S_{n0} W_{n0}) \\ U(r, \phi^f) &= \frac{\mu}{R} \sum_{n=0}^4 (C_{n0} V_{n0}) \\ &= \frac{\mu}{R} [C_{00} V_{00} + C_{10} V_{10} + C_{20} V_{20} + C_{30} V_{30} + C_{40} V_{40}] \\ &= \frac{\mu}{R} \left[\left(\frac{R}{r}\right) - J_2 \left(\frac{R}{r}\right)^3 P_2(\sin \phi^f) \right. \\ &\quad \left. - J_3 \left(\frac{R}{r}\right)^4 P_3(\sin \phi^f) - J_4 \left(\frac{R}{r}\right)^5 P_4(\sin \phi^f) \right] \quad (3.10) \\ U(r, \phi^f) &= \frac{\mu}{r} \left[1 - J_2 \left(\frac{R}{r}\right)^2 P_2(\sin \phi^f) \right. \\ &\quad \left. - J_3 \left(\frac{R}{r}\right)^3 P_3(\sin \phi^f) - J_4 \left(\frac{R}{r}\right)^4 P_4(\sin \phi^f) \right] \\ U(r, \phi^f) &= \frac{\mu}{r} \left[1 - \sum_{n=2}^4 J_n \left(\frac{R}{r}\right)^n P_n(\sin \phi^f) \right] \end{aligned}$$

Among the zonal coefficients, J_2 is by far the most significant, and dominates the non-spherical effects. It captures the Earth's oblateness and produces the well known secular perturbations in the orbital elements, which drifts the right ascension of the ascending node and rotation of the argument of perigee. The higher-degree J_3 and J_4 terms are several orders of magnitude less significant, but still produce a notable perturbation. J_3

induces long-period variations in eccentricity due to asymmetry between the northern and southern hemispheres, while J_4 refines the flatness modelling, and contributes to small corrections to the secular rates caused by J_2 [13, 21, 22]. Inserting this truncated spherical

n	J_n	$P_n(u)$
0	-1	1
1	0	u
2	1.08263×10^{-3}	$\frac{1}{2}(3u^2 - 1)$
3	-2.53266×10^{-6}	$\frac{1}{2}(5u^3 - 3u)$
4	-1.61962×10^{-6}	$\frac{1}{8}(35u^4 - 30u^2 + 3)$

Table 3.2.1: Zonal coefficients and associated Legendre polynomials up to fourth degree. Values courtesy of [23].

harmonic expression into equation 3.7 yields the acceleration experienced by an arbitrary spacecraft, expressed in the ECEF frame. By computing the gradient, then applying the time-varying transformation in equation 3.4, the acceleration can then be transformed into the ECI frame:

$$\mathbf{a}_{grav}^f = (\ddot{\mathbf{r}}_{s/i}^f)_{grav} = \nabla U(r, \phi^f) \iff \mathbf{a}_{grav}^i = (\ddot{\mathbf{r}}_{s/i}^i)_{grav} = \mathbf{R}_f^i \nabla U(r, \phi^f) \quad (3.11)$$

3.2.2 Atmospheric Drag

Atmospheric drag is the most influential non-gravitational perturbation acting on satellites in LEO. The perturbation is caused by a momentum exchange between the spacecraft's surface and the residual air-molecules encountered along its trajectory. The resulting acceleration will always act opposite to the satellite's velocity, causing a slow deceleration over time. The momentum exchange is typically modelled in the free-molecular flow regime, which assumes that the molecules bouncing off the spacecraft's surface do not interfere with incoming ones. The acceleration can then be expressed using the classical aerodynamic formulation [21, 13]:

$$\mathbf{a}_{drag}^i = (\ddot{\mathbf{r}}_{s/i}^i)_{drag} = -\frac{1}{2} C_D \frac{A_D}{m} \rho v_{rel}^2 \hat{\mathbf{v}}_{rel}^i \quad (3.12)$$

In this expression, A_D is the cross-section of the spacecraft perpendicular to the incoming molecular flow, which is often approximated as constant even though it varies with the spacecraft's attitude and geometry [22]. Furthermore, the acceleration magnitude is inversely proportional to the spacecraft's mass m , given by the area-to-mass ratio. The term \mathbf{v}_{rel}^i represents the relative velocity between the satellite and the surrounding atmosphere expressed in ECI. v_{rel} and $\hat{\mathbf{v}}_{rel}^i$ is the velocity's magnitude and unit vector, respectively. Montenbruck & Gill presents a satisfactory first-order approximation where the atmosphere co-rotates with the Earth [21]:

$$\mathbf{v}_{rel}^i = \mathbf{v}_{s/i}^i - \boldsymbol{\omega}_{f/i}^i \times \mathbf{r}_{s/i}^i, \quad (3.13)$$

where $\{\mathbf{r}_{s/i}^i, \mathbf{v}_{s/i}^i\}$ is the position and velocity of an arbitrary satellite s in ECI, and $\boldsymbol{\omega}_{f/i}^i$ is the Earth's angular velocity. The parameter ρ denotes the local atmospheric density, and its modelling is a major source of drag uncertainty because the upper atmosphere is

subject to constant change from solar and geomagnetic activity. A "rough estimate" of the density's dependence on the altitude h is the exponential density model [21, 13]:

$$\rho(h) = \rho_0 \exp\left(-\frac{h - h_0}{H_0}\right), \quad H_0 = \frac{\mathcal{R}T}{\mu_m g} \quad (3.14)$$

Here h_0 is the geocentric distance to the Earth's surface, h is the conventional altitude and ρ_0 is the reference density at altitude $h = 0$. H_0 is the density scale height, and is defined as the height where the density is reduced to ρ_0/e . This height is given as a function of Boltzmann's constant \mathcal{R} , the atmospheric temperature T , the mean molecular mass μ_m and the acceleration magnitude due to gravity g [21, 24].

The final parameter in equation 3.12 is the drag coefficient C_D . It describes the interaction between the impacting atmospheric molecule and the spacecraft's surface. Its value is dependent on the surface material, gas-surface interaction, temperature and flow regime through complex mechanisms, which makes its calculation non-trivial. However, Montenbruck & Gill reports that typical values of C_D range between 1.5 – 3.0, and that the initial estimation is commonly corrected through orbit determination [21].

3.2.3 Solar Radiation Pressure

SRP becomes the dominant non-gravitational orbital perturbation acting on a spacecraft for altitudes greater than approximately 800km. Its influence manifests as long-period variations of the orbital eccentricity, argument of perigee and inclination, especially for satellites with a large area-to-mass ratio. SRP exerts a small force through the absorption or reflection of photons. Both mechanisms transfer momentum from the photons to the surface, generating force proportional to the solar flux and directed away from the Sun. As described by Montenbruck & Gill, the resulting acceleration depends on the geometry between the Sun direction vector $\mathbf{r}_{Sun/s}^i$ and the unit vector normal to the spacecraft's flat surface $\hat{\mathbf{n}}_s$ [21]:

$$\mathbf{a}_{SRP}^i = (\ddot{\mathbf{r}}_{s/i}^i)_{SRP} = -P_{Sun} \frac{\text{AU}^2}{\|\mathbf{r}_{Sun/s}^i\|_2^2} \frac{A_R}{m_s} \cos(\theta) [(1 - \varepsilon)\hat{\mathbf{r}}_{Sun/s}^i + 2\varepsilon \cos(\theta)\hat{\mathbf{n}}_s] \quad (3.15)$$

P_{Sun} is the radiation pressure given by the solar flux at one Astronomical Unit (AU), which is defined as mean radius of Earth's orbit. Numerical values for this radiation pressure and one AU in meters is show table .0.1. $\{\mathbf{r}_{Sun/s}^i, \hat{\mathbf{r}}_{Sun/s}^i\}$ is the Sun's position relative to the satellite and its corresponding unit vector, respectively. A_R/m_s is the ratio between the cross-section area perpendicular to $\hat{\mathbf{r}}_{Sun/s}^i$ and the satellite's mass. θ represents the angle between the incoming radiation $\hat{\mathbf{r}}_{Sun/s}^i$ and n_s , and ε represents the surface reflectivity. However, Montenbrock & Gill argues that the assumption $\theta = 0$ is sufficient for many applications. Using this assumption, equation 3.15 can be simplified to the so-called "cannonball" model by introducing a radiation pressure coefficient $C_R = 1 - \varepsilon$ [21]:

$$\mathbf{a}_{SRP}^i = (\ddot{\mathbf{r}}_{s/i}^i)_{SRP} = -P_{Sun} C_R \frac{A_R}{m_s} \frac{\mathbf{r}_{Sun/s}^i}{\|\mathbf{r}_{Sun/s}^i\|_2^3} \text{AU}^2 \quad (3.16)$$

3.2.4 Third-Body Perturbations

In addition to the Earth's gravity field, a satellite in orbit around Earth also experiences gravitational pull from the Sun and Moon, causing a perturbing acceleration. Although these bodies are distant, their great masses still produce accelerations comparable to higher-order geopotential terms, especially for satellites in Medium Earth Orbit (MEO) or higher. As described by Montenbruck & Gill, the perturbing acceleration from a massive third-body B is obtained by subtracting its acceleration on the Earth from its acceleration on the spacecraft through Newton's gravitational law [21]. Its formulation in the ECI frame is:

$$\mathbf{a}_B^i = (\ddot{\mathbf{r}}_{s/i}^i)_B = \mu_B \left(\frac{\mathbf{r}_{B/i}^i - \mathbf{r}_{s/i}^i}{\|\mathbf{r}_{B/i}^i - \mathbf{r}_{s/i}^i\|_2^3} - \frac{\mathbf{r}_{B/i}^i}{\|\mathbf{r}_{B/i}^i\|_2^3} \right) = \mu_B \left(\frac{\mathbf{r}_{B/s}^i}{\|\mathbf{r}_{B/s}^i\|_2^3} - \frac{\mathbf{r}_{B/i}^i}{\|\mathbf{r}_{B/i}^i\|_2^3} \right) \quad (3.17)$$

Here $\mu_B = GM_B$ is the massive body's gravitational parameter, $\mathbf{r}_{B/s}^i$ is the body's position relative to the satellite, and $\{\mathbf{r}_{B/i}^i, \mathbf{r}_{s/i}^i\}$ denote the geocentric coordinates of the body and satellite, respectively. This differential formulation in equation 3.17 ensures that only the perturbing acceleration is expressed. Furthermore, Montenbruck & Gill explains how the perturbing gravitational attraction on a satellite changes direction relative to the Earth during its orbit. The tidal forces cause the satellite to experience a pull away from Earth whenever it is on the imaginary line striking through the Earth and the massive body, and a pull towards Earth whenever it is perpendicular to this line [21]. This effect is visualized by the "Earth-Centered Frame" in figure 3.2.2.

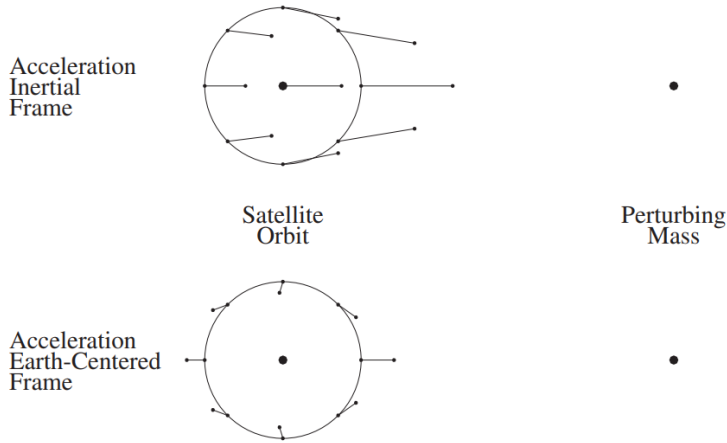


Figure 3.2.2: Tidal forces due to the gravitational attraction of a distant point-like mass. Courtesy of [21]

The total perturbing acceleration $\mathbf{a}_{B,\text{tot}}^i$ on a satellite from multiple massive bodies, like the Sun and Moon, can be found by summing multiple instances of equation 3.17 with their corresponding distances and gravitational parameters:

$$\mathbf{a}_{B,\text{tot}}^i = \mathbf{a}_{\text{Sun}}^i + \mathbf{a}_{\text{Moon}}^i \quad (3.18)$$

3.3 Numerical Orbit Propagation

3.4 Analytical Orbit Propagation - SGP4

CHAPTER
FOUR

METHODS

4.1 Simulation Design

4.2 Literature Search Methodology

4.3 Software Development

4.3.1 Software Architecture

This section is just for me to organize my thoughts while I work on developing the software architecture.

4.3.1.1 Main Pipeline

Sequential steps executed by the main program.

1. Initialize the simulation environment with global satellite instances and simulation parameters from config.
2. Call a function to run the SGP4 propagator from "GNSS_R_System_Simulator".
 - (a) Its initial conditions are the TLEs and the initial epoch, fetched from the satellite instances (from config).
 - (b) This function call also extracts the states (\vec{r} and \vec{v}) at the initial epoch in the SGP4 output frame (TEME, I believe).

- (c) The function call then transforms the states to the Basilisk inertial frame ($\text{TEME}(?) \rightarrow \text{ECI}(?)$) and adds it to the satellite instances.
 - (d) Log the output trajectories in an external file or standardized data structure for later use.
3. Call a function to run the dynamical Basilisk simulation.
- (a) Its initial conditions are the states from the SGP4 output at the initial epoch, fetched from the satellite instances.
 - (b) Log the output trajectories in an external file or standardized data structure for later use.

4.3.1.2 Config

This subsection describes all the fields included in the config file

- SIMULATION (This will contain all the high-level simulation parameters that are global for all simulation frameworks)
 - `startTime` (Real-world date and time of the simulation start. Is this different from "initial epoch"?)
 - `simulationDuration` (How long period into the future the simulation will simulate)
- SATELLITE (This will contain all the satellite-specific parameters, and there will be one such section for each satellite in the simulation)
 - `satelliteName` (A string identifier for the satellite)
 - `TLELine1` (The first line of the TLE data for the satellite)
 - `TLELine2` (The second line of the TLE data for the satellite)
 - `initialEpoch` (The epoch time corresponding to the TLE data, in a standardized format. Should always be the same as `startTime`???)
 - physical attributes like size, mass, drag coefficient, inertia, etc. (TBD!)
- PLOTTING (This will contain all the parameters related to how the simulation results should be visualized)
 - `savePath` (Path to save the generated plots)
 - Other plotting parameters (TBD!)
- SKYFIELD (This will contain all the parameters specific to the Skyfield simulation)
 - `timeStep` (The time step for the Skyfield simulation)
 - Skyfield-specific parameters (TBD!)
- BASILISK (This will contain all the parameters specific to the Basilisk simulation framework)

- `timeStep` (The time step for the Basilisk simulation)
- `solver` (The numerical solver to be used in the Basilisk simulation)
- `gravityModel` (The gravity model to be used in the Basilisk simulation)
- `radiationPressureModel` (The radiation pressure model to be used in the Basilisk simulation)
- Other Basilisk-specific parameters (TBD!)

The below list shows additional capabilities in Basilisk that have yet to be implemented, but could serve to increase the fidelity of the simulation.

- Track a point relative to the satellite's COM

CHAPTER
FIVE

RESULTS

5.1 Simulation Parameters

Parameter	Value	Unit
C_D	1.5 – 3	-
A_D	-	-
C_R	-	-
A_{SRP}	-	-

Table 5.1.1: Physical constants and associated numerical value. J -terms courtesy of [23].

5.2 Prelim results

The current simulator implementation has been used to generate preliminary results for a two-satellite scenario consisting of one chief and one follower spacecraft initialized on different orbital planes in LEO. Skyfield’s SGP4 model serves as the baseline, while the Basilisk simulation includes gravity-gradient effects, solar radiation pressure, and lunar third-body pull. Atmospheric drag has not yet been implemented, and both propagators are run over the same integration time for direct comparison.

Figure 1 and 2 show the ECI position and velocity differences between Basilisk and SGP4 for the chief and follower spacecraft, respectively. Figure 3 presents the difference in relative motion between the two spacecraft expressed in the RTN frame. In all cases, the divergence begins small but increases steadily over time. This divergence can be attributed to a combination of intrinsic numerical simulator difference and additional physical perturbations included only in the Basilisk simulation. The large discrepancy

visible in the relative-motion plot indicates that a formation-keeping delta-V analysis performed with the two simulation frameworks would yield significantly different results after 24 hours. Further testing and analysis are required to determine how much of this divergence is caused by numerical effects versus physical modelling differences.

Below is a list over all types of plots that I deem valuable for the specialization project. Each plot-type shall be justified by a short description of its usefulness.

5.2.1 Simulator output difference plots

Show the absolute value logarithmic difference between the simulators. This will make it easier to see the small differences for times smaller than 6 hours, and the big differences after 24 hours. Do this for both the absolute pos/vel difference plot, and the relative formation pos/vel plots.

5.2.2 R

CHAPTER
SIX

DISCUSSION

Discuss your results here.

6.1 Future work

Include a section about what should or could be done in future research, or explain any recommended next steps based on the results you got. This should be the last section in the discussion.

How do zxc here's to all the idk This situation is starting to become pretty dire

CHAPTER
SEVEN

CONCLUSIONS

Give a concise summary of your research and finding here, and include a short summary of any future work as well.

REFERENCES

- [1] NASA Earthdata. *GNSS - Global Navigation Satellite System*. Accessed: 2025-11-23. 2024. URL: <https://www.earthdata.nasa.gov/data/space-geodesy-techniques/gnss>.
- [2] Harry W. Jones. “The Recent Large Reduction in Space Launch Cost”. In: *48th International Conference on Environmental Systems (ICES)*. ICES-2018-81. Albuquerque, New Mexico, July 2018, pp. 1–10. URL: <https://ntrs.nasa.gov/citations/20200001093>.
- [3] *Hva er jamming, spoofing og meaconing?* FFI Factsheet. Accessed: 2025-11-21. Norwegian Defence Research Establishment (FFI), 2024.
- [4] Norwegian Defence Research Establishment (FFI). *Jamming - a technological cat-and-mouse game*. <https://www.ffi.no/en/news/jamming--a-technological-cat-and-mouse-game>. Accessed: 2025-02-20. 2024.
- [5] GPSJam Project. *GPSJam - Real-time GNSS Interference Map*. <https://gpsjam.org>. Accessed: 2025-11-21. 2025.
- [6] Shuanggen Jin and Attila Komjathy. “GNSS Reflectometry and Remote Sensing: New Objectives and Results”. In: *Advances in Space Research* 46.1 (2010), pp. 111–117. DOI: [10.1016/j.asr.2010.01.014](https://doi.org/10.1016/j.asr.2010.01.014). URL: https://www.sciencedirect.com/science/article/pii/S0273117710000499?casa_token=0z4kQjAlYwsAAAAA:STxQm3Wyqd2XvnpbveQhRXNvqU0fPIugKy2wwwYIkM65IhS2z184e07fH4z2QJhcTMW1f3IT.
- [7] C. Hall and R. Cordey. “Multistatic Scatterometry”. In: *Proceedings of the IEEE International Geoscience and Remote Sensing Symposium (IGARSS)*. IEEE. Edinburgh, Scotland, 1988, pp. 561–562.
- [8] NTNU SmallSat Lab. *CubeSat Concept Using GNSS-R*. <https://www.ntnu.edu/smallsat/gnss-r>. Accessed: 2025-11-21. 2025.
- [9] Scott Gleason et al. “Geolocation, Calibration and Surface Resolution of CYGNSS GNSS-R Land Observations”. In: *Remote Sensing* 12.8 (2020), p. 1317. DOI: [10.3390/rs12081317](https://doi.org/10.3390/rs12081317). URL: <https://www.mdpi.com/2072-4292/12/8/1317>.
- [10] Saika Aida and Michael Kirschner. “Accuracy Assessment of SGP4 Orbit Information Conversion into Osculating Elements”. In: (2013). Retrieved from user-provided document, pp. 1–8. URL: <https://elib.dlr.de/87081>.
- [11] Victor Szebehely. “The History and Background of Astrodynamics”. In: *Acta Astronautica* 20 (1989), pp. 79–81.

- [12] Isaac Newton. *Philosophiae Naturalis Principia Mathematica*. Londini: Jussu Societatis Regiae ac Typis Josephi Streater, 1687.
- [13] David A. Vallado. *Fundamentals of Astrodynamics and Applications*. Springer, 2001. URL: <https://books.google.no/books?id=PJL1WzMBKjkC>.
- [14] Zac Yung-Chun Liu et al. “Improved Orbital Propagator Integrated with SGP4 and Machine Learning”. In: *AIAA/USU Small Satellite Conference*. 2021. URL: <https://digitalcommons.usu.edu/smallsat/2021/all2021/193>.
- [15] Dave Conkey and Mitchell Zielinski. “Assessing Performance Characteristics of the SGP4-XP Propagation Algorithm”. In: *Advanced Maui Optical and Space Surveillance Technologies Conference (AMOS)*. 2022. URL: <https://amostech.com/TechnicalPapers/2022/Poster/Conkey.pdf>.
- [16] Giacomo Acciarini, Atilim Günes Baydin, and Dario Izzo. “Closing the Gap Between SGP4 and High-Precision Propagation via Differentiable Programming”. In: *Acta Astronautica* (2024). URL: <https://www.sciencedirect.com/science/article/pii/S0094576524006374>.
- [17] Mariusz Eivind Grøtte et al. “Spacecraft Attitude and Angular Rate Tracking using Reaction Wheels and Magnetorquers”. In: *IFAC-PapersOnLine* 53.2 (2020), pp. 14819–14826. DOI: [10.1016/j.ifacol.2020.12.1924](https://doi.org/10.1016/j.ifacol.2020.12.1924). URL: <https://www.sciencedirect.com/science/article/pii/S2405896320325441>.
- [18] Gabriel Popescu. “Pixel Geolocation Algorithm for Satellite Scanner Data”. In: (2014). PDF provided by user; publication year and journal not specified. URL: https://www.researchgate.net/publication/311807426_Pixel_geolocation_algorithm_for_satellite_scanner_data.
- [19] Sascha Metz. “Implementation and Comparison of Data-Based Methods for Collision Avoidance in Satellite Operations”. Master’s Thesis. Darmstadt, Germany: Technische Universität Darmstadt, 2020. URL: https://www.researchgate.net/publication/344268107_Master_Thesis_Implementation_and_comparison_of_data-based_methods_for_collision_avoidance_in_satellite_operations.
- [20] John Stryjewski. *Coordinate Transformations*. Technical Report. Version 08/19/20. MIT Lincoln Laboratory, Aug. 2020. URL: https://x-lumin.com/wp-content/uploads/2020/09/Coordinate_Transforms.pdf.
- [21] Oliver Montenbruck and Eberhard Gill. *Satellite Orbits: Models, Methods and Applications*. 1st ed. Corrected 4th printing 2012. Berlin, Heidelberg: Springer, 2000. ISBN: 978-3-540-67280-7. URL: https://ftp.space.dtu.dk/pub/nio/Macau/Montenbruck_2000_SatelliteOrbits.pdf.
- [22] Christopher W. T. Roscoe et al. “Force Modeling and State Propagation for Navigation and Maneuver Planning for CubeSat Rendezvous, Proximity Operations, and Docking”. In: *Proceedings of the AAS/AIAA Spaceflight Mechanics Meeting*. Applied Defense Solutions. Columbia, Maryland, 2014. URL: <https://www.scopus.com/pages/publications/84898934271?origin=resultslist>.
- [23] Weichao Zhong and Pini Gurfil. “Mean Orbital Elements Estimation for Autonomous Satellite Guidance and Orbit Control”. In: *Journal of Guidance, Control, and Dynamics* 36.6 (2013), pp. 1624–1641. DOI: [10.2514/1.60701](https://doi.org/10.2514/1.60701). URL: https://www.researchgate.net/publication/260501946_Mean_Orbital_Elements_Estimation_for_Autonomous_Satellite_Guidance_and_Orbit_Control.

- [24] Australian Space Academy. *Terrestrial Atmosphere Modelling*. <https://www.spaceacademy.net.au/watch/debris/atmosmod.htm>.

APPENDICES

A - GITHUB REPOSITORY

All code and latex-files used in this document are included in the Github repository linked below. Further explanations are given in the readme-file.

Specialization project report LaTeX repository link

- <https://github.com/chystad/Specialization-Project-Report-LaTeX->

Orbit Simulator repository link

- https://github.com/chystad/Orbit_Simulator

B - NUMERICAL VALUES

Numerical Values for Physical Constants

<i>Constant</i>	<i>Value</i>	<i>Unit</i>
J_0	-1	-
J_1	0	-
J_2	1.08263×10^{-3}	-
J_3	-2.53266×10^{-6}	-
J_4	-1.61962×10^{-6}	-
P_{Sun}	$4.578299965 \times 10^{-6}$	Ws/m^3
$1AU$	149597871	km
—	—	—
—	—	—
—	—	—
—	—	—
—	—	—
—	—	—

Table .0.1: Physical constants and associated numerical value. J -terms courtesy of [23].